

Image-Domain Tilt Constrained Distributed Fusion for Maneuvering UAV Tracking with Multi-Camera Electro-Optical Observations

Minxing Sun and Yao Mao

Abstract

Short-horizon prediction is essential for electro-optical UAV tracking, especially when the target is small, maneuvering, or intermittently observed. Image center, line-of-sight, and range measurements provide direct constraints on target position, but their constraints on acceleration are weak. As a result, prediction can lag during aggressive maneuvers.

This paper proposes an image-domain tilt constrained distributed fusion method for maneuvering UAV tracking. The method uses the apparent roll and pitch of a rotorcraft target in the image as low-level maneuver cues. A weak-prior auto-labeling pipeline first generates oriented bounding box and image-domain tilt labels from synchronized video, gimbal IMU, and UAV IMU data. A YOLO-OBB detector is then trained to provide online target position and tilt measurements. The front-end Python implementation is publicly available at <https://github.com/ShineMinxing/PythonYOLO>.

In the fusion stage, the UAV state is modeled by position, velocity, and acceleration. Image-domain roll and pitch are introduced as acceleration-related pseudo-observations. For distributed tracking, one mobile gimbal camera and two fixed ground cameras are fused asynchronously. Camera attitude error states are augmented into the filter to absorb extrinsic drift and cross-camera systematic inconsistency. A Mahalanobis gate with time-since-last-valid covariance widening is used to reject false detections and handle dropouts.

In simulation, adding roll/pitch observations reduces the prediction RMSE from 1.991 m to 0.821 m and decreases the cumulative prediction error by 60.75%. In real distributed experiments, a self-consistency evaluation shows an 18.10% reduction in cumulative prediction error. The results show that image-domain tilt can provide useful acceleration constraints for robust short-horizon UAV prediction.

Minxing Sun and Yao Mao are with the Institute of Optics and Electronics, Chinese Academy of Sciences, Chengdu, China. Minxing Sun is also with the Institute for Infocomm Research (I²R), Agency for Science, Technology and Research, Singapore, and Shenzhen Astralldynamics Technology.

Corresponding email: sunminxing20@mails.ucas.ac.cn, maoyao@ioe.ac.cn.

Index Terms

UAV tracking, electro-optical tracking, image-domain tilt, YOLO-OBB, distributed fusion, multi-camera tracking, unscented Kalman filter

I. INTRODUCTION

Small UAVs have been widely used in inspection, emergency response, public safety, and low-altitude operation scenarios. Their increasing density and task diversity also bring new requirements for low-altitude monitoring, key-area protection, and safety management. In these applications, a tracking system is expected not only to detect the target, but also to continuously output stable target states for pointing control, cooperative observation, and short-horizon prediction.

Electro-optical tracking is an important part of low-altitude monitoring systems because optical sensors provide high angular resolution and rich appearance information. In practical systems, optical tracking is often combined with radar, radio-frequency, acoustic, or other wide-area sensors to form a coarse-to-fine monitoring chain [1]. After the target enters the optical tracking stage, the key problem becomes whether the system can maintain a stable closed loop of image measurement, state estimation, prediction, and servo pointing. This closed loop is affected by image noise, target scale variation, motion blur, background clutter, vibration, atmospheric disturbance, processing latency, and communication delay [2], [3], [4], [5], [6], [7]. Therefore, the state estimator must provide a prediction that is aligned with the control or fusion time, rather than only smoothing past measurements.

UAV image detection has been extensively studied with deep neural networks. Two-stage detectors such as Faster R-CNN provide strong region-level detection capability, while one-stage detectors represented by the YOLO family are more suitable for real-time deployment [8], [9], [10]. For UAV monitoring, bird-like distractors, small target size, low contrast, and changing backgrounds remain important causes of false detections and missed detections [9], [11], [12]. Existing works improve detection robustness through transfer learning, lightweight network design, data augmentation, infrared information, and multi-dataset training [13], [14], [15], [16]. However, a detector output becomes useful for electro-optical tracking only after it is converted into reliable measurements for state estimation and prediction.

Classical recursive estimators, including Kalman filtering and its nonlinear variants, provide a clear state-space framework for target tracking [17], [18], [19]. For nonlinear optical measurements, extended Kalman filtering, unscented Kalman filtering, cubature Kalman filtering, and particle filtering have been widely investigated [19], [20], [21], [22], [23], [24], [25], [26], [27]. For maneuvering targets, multiple-model methods such as IMM improve adaptability by maintaining several motion hypotheses [28], [29], [30]. Robust and adaptive filters further address model mismatch, time-varying noise, and outliers by

covariance adaptation, residual reweighting, or statistical gating [31], [32], [33], [34], [35], [36], [37], [38]. Nevertheless, most optical tracking filters still rely mainly on position-like measurements, such as image center, line-of-sight direction, and range. These measurements directly constrain target position, but only indirectly constrain velocity and acceleration. When the target maneuvers quickly or short dropouts occur, the acceleration estimate can lag, and the prediction error can be amplified.

Rotorcraft UAVs provide an additional physical cue. Their apparent roll and pitch are related to the thrust direction and therefore to the horizontal acceleration tendency. Although image-domain tilt is not an exact body attitude measurement, it contains useful maneuver information. This paper uses this cue as an acceleration-related pseudo-observation. Different from methods that only improve the detector, the proposed method couples image-domain tilt recognition with a distributed state estimator.

Distributed observation is also important for low-altitude UAV tracking. Multi-node systems can reduce blind areas and improve geometric observability, but they introduce asynchronous sampling, heterogeneous observation quality, communication delay, and cross-camera calibration inconsistency [39]. Mobile observation platforms further increase flexibility in complex terrain. Legged or wheel-legged robots can carry optical sensors to viewpoints that are difficult for fixed stations or conventional wheeled vehicles to reach [40], [41], [42]. In this work, one mobile gimbal camera and two fixed ground cameras are fused in a unified state-space model. Camera attitude error states are introduced to compensate residual extrinsic inconsistency, and a per-camera Mahalanobis gate is used to handle false detections and dropouts.

The main contributions are:

- **Weak-prior tilt labeling for UAV images.** A video-IMU auto-labeling pipeline is constructed to generate UAV oriented bounding boxes and image-domain roll/pitch labels without manual frame-by-frame OBB annotation.
- **Acceleration-constrained prediction filtering.** Image-domain roll and pitch are modeled as pseudo-observations related to target acceleration, improving acceleration observability during maneuvers and short missing intervals.
- **Asynchronous distributed multi-camera fusion.** One mobile gimbal camera and two fixed cameras are fused in a unified state-space model. Camera attitude error states are augmented to improve cross-camera consistency.
- **Robust update under dropouts and false detections.** A per-camera Mahalanobis gate with time-since-last-valid covariance widening is used to reject hard outliers and down-weight suspicious observations.
- **Public front-end implementation.** The Python workflow for motion point extraction, target tracing,

weak label generation, and YOLO-OBb training is released at <https://github.com/ShineMinxing/PythonYOLO>.

The remainder of this paper is organized as follows. Section II defines the observation model. Section III presents weak-prior labeling and YOLO-OBb training. Section IV introduces the tilt-constrained distributed fusion method. Section V reports simulation and real experiments. Section VII concludes the paper.

II. SYSTEM AND OBSERVATION MODEL

A. System Composition

The system contains observation nodes, a UAV target, and a processing node. During weak-prior label generation, the observation node is a gimbal camera with an IMU, and the target UAV also records IMU data. During distributed fusion, the observation network contains three cameras: Cam1 is a mobile gimbal camera mounted on a quadruped robot, and Cam2/Cam3 are fixed ground cameras.

Let the k -th image be \mathbf{I}_k . The synchronized gimbal IMU and UAV IMU measurements are denoted by \mathbf{m}_k^G and \mathbf{m}_k^U . The weak-prior dataset is

$$\mathcal{D} = \{(\mathbf{I}_k, \mathbf{m}_k^G, \mathbf{m}_k^U)\}_{k=1}^N. \quad (1)$$

For online fusion, the mobile camera pose is computed from robot odometry, the static transform from the robot body to the gimbal, gimbal encoder readings, and the camera-gimbal transform. The two fixed cameras use calibrated initial extrinsics. Residual attitude errors are estimated online as augmented states.

B. Camera Geometry

We use a world frame $\{W\}$ and camera frames $\{C_i\}$, $i = 1, 2, 3$. For camera i , its world position is $\mathbf{c}_w^{(i)}$, and its attitude is ${}^W\mathbf{R}_{C_i}$. For target position $\mathbf{p}_w = [X_w, Y_w, Z_w]^T$, the target coordinate in the camera frame is

$$\mathbf{p}_c^{(i)} = ({}^W\mathbf{R}_{C_i})^T (\mathbf{p}_w - \mathbf{c}_w^{(i)}) = \begin{bmatrix} X_c^{(i)} & Y_c^{(i)} & Z_c^{(i)} \end{bmatrix}^T. \quad (2)$$

The azimuth, elevation, and range are

$$\begin{aligned} \alpha^{(i)} &= \text{atan2}(Y_c^{(i)}, X_c^{(i)}), \\ \epsilon^{(i)} &= \text{atan2}\left(Z_c^{(i)}, \sqrt{(X_c^{(i)})^2 + (Y_c^{(i)})^2}\right), \\ \rho^{(i)} &= \sqrt{(X_c^{(i)})^2 + (Y_c^{(i)})^2 + (Z_c^{(i)})^2}. \end{aligned} \quad (3)$$

In the MATLAB simulation, angular coordinates are mapped to image coordinates by the field-of-view model

$$u^{(i)} = \frac{W_{\text{img}}}{2} + \frac{\alpha^{(i)}}{\Theta_x^{(i)}} W_{\text{img}}, \quad v^{(i)} = \frac{H_{\text{img}}}{2} + \frac{\epsilon^{(i)}}{\Theta_y^{(i)}} H_{\text{img}}, \quad (4)$$

where $W_{\text{img}} = 1920$, $H_{\text{img}} = 1080$, and $\Theta_x^{(i)}, \Theta_y^{(i)}$ are the horizontal and vertical fields of view.

Each camera provides a five-dimensional observation block:

$$\mathbf{z}_k^{(i)} = \left[u_k^{(i)} \quad v_k^{(i)} \quad \rho_k^{(i)} \quad \eta_{\text{roll},k}^{(i)} \quad \eta_{\text{pitch},k}^{(i)} \right]^T. \quad (5)$$

The stacked three-camera observation is

$$\mathbf{z}_k = \left[\mathbf{z}_k^{(1)T} \quad \mathbf{z}_k^{(2)T} \quad \mathbf{z}_k^{(3)T} \right]^T \in \mathbb{R}^{15}. \quad (6)$$

C. Image-Domain Tilt

Let the line-of-sight unit vector in the camera frame be

$$\boldsymbol{\ell}_c^{(i)} = \frac{\mathbf{p}_c^{(i)}}{\|\mathbf{p}_c^{(i)}\|}. \quad (7)$$

Equivalently, using the field-of-view mapping,

$$\psi^{(i)} = \frac{u^{(i)} - W_{\text{img}}/2}{W_{\text{img}}} \Theta_x^{(i)}, \quad \vartheta^{(i)} = \frac{v^{(i)} - H_{\text{img}}/2}{H_{\text{img}}} \Theta_y^{(i)}, \quad (8)$$

$$\boldsymbol{\ell}_c^{(i)} = \begin{bmatrix} \cos \vartheta^{(i)} \cos \psi^{(i)} \\ \cos \vartheta^{(i)} \sin \psi^{(i)} \\ \sin \vartheta^{(i)} \end{bmatrix}. \quad (9)$$

The local image-plane right and up bases are

$$\mathbf{e}_r^{(i)} = \frac{\begin{bmatrix} -\sin \psi^{(i)} & \cos \psi^{(i)} & 0 \end{bmatrix}^T}{\left\| \begin{bmatrix} -\sin \psi^{(i)} & \cos \psi^{(i)} & 0 \end{bmatrix}^T \right\|}, \quad \mathbf{e}_u^{(i)} = \frac{\mathbf{e}_r^{(i)} \times \boldsymbol{\ell}_c^{(i)}}{\left\| \mathbf{e}_r^{(i)} \times \boldsymbol{\ell}_c^{(i)} \right\|}. \quad (10)$$

Given an equivalent UAV normal vector $\mathbf{n}_c^{(i)}$ in camera i , the image-domain roll and pitch are defined as

$$\begin{aligned} \eta_{\text{roll}}^{(i)} &= \text{wrap} \left[\text{atan2} \left(\mathbf{n}_c^{(i)T} \mathbf{e}_r^{(i)}, \mathbf{n}_c^{(i)T} \mathbf{e}_u^{(i)} \right) \right], \\ \eta_{\text{pitch}}^{(i)} &= -\arcsin \left(\text{clip} \left(\mathbf{n}_c^{(i)T} \boldsymbol{\ell}_c^{(i)}, -1, 1 \right) \right). \end{aligned} \quad (11)$$

These angles are treated as noisy image-domain maneuver cues rather than exact UAV body attitude.

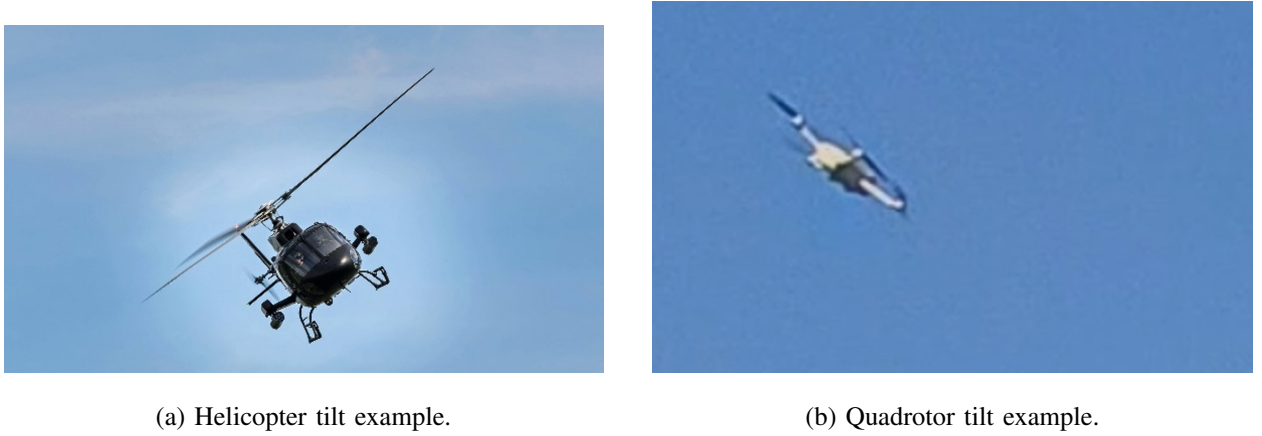


Fig. 1. Image-domain body tilt contains short-term maneuver tendency information.

III. WEAK-PRIOR AUTO-LABELING AND YOLO-OBB TILT RECOGNITION

A. Overview

The purpose of the front end is to obtain continuous target position and tilt measurements without manually labeling large numbers of OBB samples. The workflow contains four steps: motion candidate extraction, target trajectory association, weak roll/pitch label generation, and YOLO-OBB training.

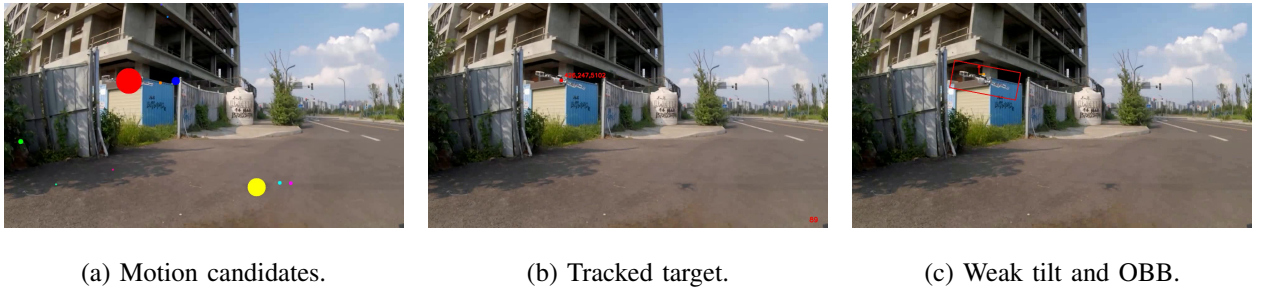


Fig. 2. Main steps of the weak-prior auto-labeling pipeline.

B. Motion Candidate Extraction

For each frame \mathbf{I}_k , a Gaussian mixture background model is used to obtain foreground candidates:

$$p(\mathbf{p}_{\text{pix},k}) = \sum_{i=1}^K \omega_i \mathcal{N}(\mathbf{p}_{\text{pix},k}; \boldsymbol{\mu}_i, \boldsymbol{\Sigma}_i). \quad (12)$$

A pixel is regarded as foreground if it cannot be explained by the current background model under a Mahalanobis threshold:

$$(\mathbf{p}_{\text{pix},k} - \boldsymbol{\mu}_i)^T \boldsymbol{\Sigma}_i^{-1} (\mathbf{p}_{\text{pix},k} - \boldsymbol{\mu}_i) > \tau_{\text{pix}}. \quad (13)$$

After morphology and connected-component extraction, a contour with area $A_{n,k}$ is retained if

$$A_{\min} \leq A_{n,k} \leq \rho_{\max} W_{\text{img}} H_{\text{img}}. \quad (14)$$

The retained candidate set is

$$\mathcal{P}_k = \{(x_{i,k}, y_{i,k}, A_{i,k})\}_{i=1}^{N_k}. \quad (15)$$

C. Target Trajectory Association

Let the previous target position be $\hat{\mathbf{s}}_{k-1} = [\hat{u}_{k-1}, \hat{v}_{k-1}]^T$. The distance from candidate i to the previous target is

$$\delta_{i,k} = \left\| \begin{bmatrix} x_{i,k} & y_{i,k} \end{bmatrix}^T - \hat{\mathbf{s}}_{k-1} \right\|_2. \quad (16)$$

Within a search radius r_k^{trk} , the target candidate is selected by

$$i_k^* = \arg \max_{i: \delta_{i,k} \leq r_k^{\text{trk}}} (A_{i,k}, -\delta_{i,k}). \quad (17)$$

If no candidate is found, the frame is marked as missing and the search radius is enlarged. Short missing segments are filled by interpolation.

D. Weak Tilt Labels from Dual IMU

The UAV IMU provides the UAV attitude ${}^W \mathbf{R}_U(k)$. The gimbal IMU and camera-gimbal calibration provide the camera attitude ${}^W \mathbf{R}_C(k)$. For a constant UAV equivalent normal vector \mathbf{n}_0^U , its camera-frame expression is

$$\mathbf{n}_k^C = ({}^W \mathbf{R}_C(k))^T {}^W \mathbf{R}_U(k) \mathbf{n}_0^U. \quad (18)$$

Together with the image target position, Eq. (11) gives weak image-domain roll/pitch labels. To remove a constant installation bias, the labels are expressed relative to the first valid frame:

$$\begin{aligned} \tilde{\eta}_{\text{pitch},k} &= \eta_{\text{pitch},k} - \eta_{\text{pitch},1}, \\ \tilde{\eta}_{\text{roll},k} &= \text{wrap}(\eta_{\text{roll},k} - \eta_{\text{roll},1}). \end{aligned} \quad (19)$$

E. Adaptive OBB Label Generation

Let the tracked target area be $A_{\text{drone},k}$. The OBB size is generated by

$$W_{\text{pix},k} = k_w \sqrt{A_{\text{drone},k}}, \quad H_{\text{pix},k} = k_h \sqrt{A_{\text{drone},k}} (1 + |\sin \tilde{\eta}_{\text{pitch},k}|). \quad (20)$$

Let $w_k = W_{\text{pix},k}/2$ and $h_k = H_{\text{pix},k}/2$. The four vertices of the unrotated box are

$$\mathbf{p}_{k,1} = \begin{bmatrix} w_k \\ h_k \end{bmatrix}, \quad \mathbf{p}_{k,2} = \begin{bmatrix} -w_k \\ h_k \end{bmatrix}, \quad \mathbf{p}_{k,3} = \begin{bmatrix} -w_k \\ -h_k \end{bmatrix}, \quad \mathbf{p}_{k,4} = \begin{bmatrix} w_k \\ -h_k \end{bmatrix}. \quad (21)$$

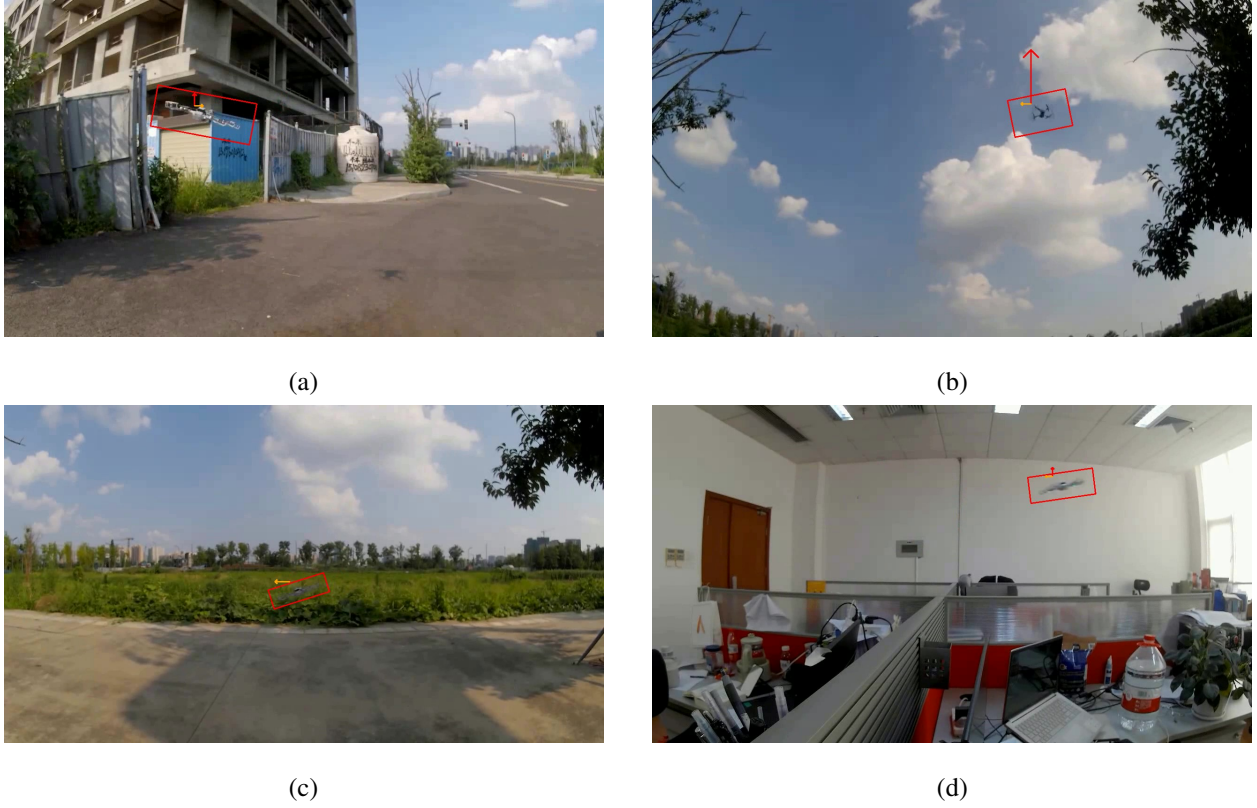


Fig. 3. Examples of weak image-domain tilt labels and adaptive OBB labels.

After rotation and translation,

$$\bar{\mathbf{p}}_{k,j} = \mathbf{R}_2(-\tilde{\eta}_{\text{roll},k}) \mathbf{p}_{k,j} + \begin{bmatrix} \hat{u}_k \\ \hat{v}_k \end{bmatrix}, \quad (22)$$

where

$$\mathbf{R}_2(\alpha) = \begin{bmatrix} \cos \alpha & -\sin \alpha \\ \sin \alpha & \cos \alpha \end{bmatrix}. \quad (23)$$

The label is exported in four-point YOLO-OBB format.

F. YOLO-OBB Training

The generated dataset is used to train a YOLO-OBB detector. The online detector outputs the UAV center, OBB geometry, and image-domain tilt cues. The detector is trained not only for frame-level recognition, but also to provide stable low-level measurements for the subsequent state estimator.

Algorithm 1 Weak-prior labeling and YOLO-OBB training

Require: Video frames, gimbal IMU, UAV IMU, camera parameters

Ensure: YOLO-OBB dataset and trained detector

- 1: **for** each frame k **do**
 - 2: Extract foreground candidates by background modeling.
 - 3: Filter contours by area and morphology.
 - 4: **end for**
 - 5: Reconstruct the UAV image trajectory by radius-constrained association.
 - 6: Interpolate short missing segments.
 - 7: **for** each valid frame k **do**
 - 8: Compute the UAV normal in the camera frame from dual-IMU geometry.
 - 9: Generate weak image-domain roll/pitch labels.
 - 10: Generate an adaptive OBB from target area and weak tilt labels.
 - 11: Export the four-point YOLO-OBB annotation.
 - 12: **end for**
 - 13: Train the YOLO-OBB detector.
-

IV. TILT-CONSTRAINED DISTRIBUTED FUSION

A. Augmented State

The target motion state is represented by position, velocity, and acceleration:

$$\mathbf{x}_k^u = \begin{bmatrix} \mathbf{p}_k^T & \mathbf{v}_k^T & \mathbf{a}_k^T \end{bmatrix}^T. \quad (24)$$

The MATLAB fusion model uses an 18-dimensional augmented state:

$$\mathbf{x}_k = [x_k, \dot{x}_k, \ddot{x}_k, y_k, \dot{y}_k, \ddot{y}_k, z_k, \dot{z}_k, \ddot{z}_k, \phi_k^{(1)}, \theta_k^{(1)}, \psi_k^{(1)}, \phi_k^{(2)}, \theta_k^{(2)}, \psi_k^{(2)}, \phi_k^{(3)}, \theta_k^{(3)}, \psi_k^{(3)}]^T. \quad (25)$$

The first nine states are the UAV motion states. The last nine states are effective camera roll-pitch-yaw states. They can be interpreted as nominal camera attitudes plus slowly varying error angles.

For each axis, the constant-acceleration propagation is

$$\begin{bmatrix} q_{k+1} \\ \dot{q}_{k+1} \\ \ddot{q}_{k+1} \end{bmatrix} = \mathbf{F}_{ca}(\Delta t_k) \begin{bmatrix} q_k \\ \dot{q}_k \\ \ddot{q}_k \end{bmatrix} + \mathbf{w}_{q,k}, \quad (26)$$

where

$$\mathbf{F}_{\text{ca}}(\Delta t_k) = \begin{bmatrix} 1 & \Delta t_k & \frac{1}{2}\Delta t_k^2 \\ 0 & 1 & \Delta t_k \\ 0 & 0 & 1 \end{bmatrix}. \quad (27)$$

The camera attitude states use random-walk propagation with small process noise.

B. Acceleration-to-Tilt Observation

For a rotorcraft UAV, horizontal acceleration is related to the direction of the thrust vector. A simplified relation is

$$\eta_{\text{pitch}} \approx \arctan\left(\frac{a_x}{g}\right), \quad \eta_{\text{roll}} \approx \arctan\left(\frac{a_y}{g}\right), \quad (28)$$

where g is the gravitational acceleration. Instead of directly converting tilt to acceleration by a tangent inverse, the filter predicts the tilt from the acceleration states. This avoids noise amplification at larger tilt angles.

In the implemented observation model, the acceleration states first define an equivalent UAV attitude:

$$\theta_u = \arctan 2(a_x, g), \quad \phi_u = \arctan 2(a_y, g), \quad \psi_u = 0. \quad (29)$$

The equivalent UAV normal vector in the world frame is

$$\mathbf{n}_w = \mathbf{R}_z(\psi_u)\mathbf{R}_y(\theta_u)\mathbf{R}_x(\phi_u) \begin{bmatrix} 0 \\ 0 \\ -1 \end{bmatrix}. \quad (30)$$

For camera i ,

$$\mathbf{n}_c^{(i)} = ({}^W\mathbf{R}_{C_i})^T \mathbf{n}_w. \quad (31)$$

The predicted roll/pitch observation is then computed by Eq. (11).

C. Observation Prediction

For each available camera, the state predicts the geometric observation

$$\hat{\mathbf{z}}_{\text{geo}}^{(i)} = \begin{bmatrix} \hat{u}^{(i)} & \hat{v}^{(i)} & \hat{\rho}^{(i)} \end{bmatrix}^T \quad (32)$$

by Eq. (2)–(4). The acceleration states predict the tilt observation

$$\hat{\mathbf{z}}_{\eta}^{(i)} = \begin{bmatrix} \hat{\eta}_{\text{roll}}^{(i)} & \hat{\eta}_{\text{pitch}}^{(i)} \end{bmatrix}^T. \quad (33)$$

Thus,

$$\hat{\mathbf{z}}^{(i)} = \begin{bmatrix} \hat{u}^{(i)} & \hat{v}^{(i)} & \hat{\rho}^{(i)} & \hat{\eta}_{\text{roll}}^{(i)} & \hat{\eta}_{\text{pitch}}^{(i)} \end{bmatrix}^T. \quad (34)$$

D. Unscented Kalman Update

The observation function contains camera projection, range geometry, angle wrapping, and acceleration-to-tilt mapping. Therefore, a sigma-point nonlinear Kalman estimator is used.

Let the state dimension be n . The sigma points are

$$\begin{aligned}\mathcal{X}_{0,k} &= \hat{\mathbf{x}}_{k|k}, \\ \mathcal{X}_{j,k} &= \hat{\mathbf{x}}_{k|k} + \left[\sqrt{(n+\lambda)\mathbf{P}_{k|k}} \right]_j, \quad j = 1, \dots, n, \\ \mathcal{X}_{j+n,k} &= \hat{\mathbf{x}}_{k|k} - \left[\sqrt{(n+\lambda)\mathbf{P}_{k|k}} \right]_j, \quad j = 1, \dots, n.\end{aligned}\tag{35}$$

After propagation through the transition and observation functions,

$$\hat{\mathbf{x}}_{k|k-1} = \sum_j W_j^{(m)} \mathcal{X}_{j,k|k-1},\tag{36}$$

$$\hat{\mathbf{z}}_{k|k-1} = \sum_j W_j^{(m)} \mathcal{Z}_{j,k}.\tag{37}$$

The innovation covariance and cross covariance are

$$\mathbf{P}_{zz} = \sum_j W_j^{(c)} (\mathcal{Z}_{j,k} - \hat{\mathbf{z}}_{k|k-1}) (\mathcal{Z}_{j,k} - \hat{\mathbf{z}}_{k|k-1})^T + \mathbf{R}_k,\tag{38}$$

$$\mathbf{P}_{xz} = \sum_j W_j^{(c)} (\mathcal{X}_{j,k|k-1} - \hat{\mathbf{x}}_{k|k-1}) (\mathcal{Z}_{j,k} - \hat{\mathbf{z}}_{k|k-1})^T.\tag{39}$$

The update is

$$\mathbf{K}_k = \mathbf{P}_{xz} \mathbf{P}_{zz}^{-1},\tag{40}$$

$$\hat{\mathbf{x}}_{k|k} = \hat{\mathbf{x}}_{k|k-1} + \mathbf{K}_k (\mathbf{z}_k - \hat{\mathbf{z}}_{k|k-1}),\tag{41}$$

$$\mathbf{P}_{k|k} = \mathbf{P}_{k|k-1} - \mathbf{K}_k \mathbf{P}_{xz}^T.\tag{42}$$

The updated state is then propagated to the prediction horizon τ .

E. Mahalanobis Gating

Before the filter update, each camera block is gated independently. The gate is applied to the geometric sub-block

$$\mathbf{z}_{\text{geo}}^{(i)} = \begin{bmatrix} u^{(i)} & v^{(i)} & \rho^{(i)} \end{bmatrix}^T.\tag{43}$$

Let the predicted geometric observation be $\hat{\mathbf{z}}_{\text{geo}}^{(i)}$. The residual is

$$\boldsymbol{\nu}_k^{(i)} = \mathbf{z}_{\text{geo},k}^{(i)} - \hat{\mathbf{z}}_{\text{geo},k}^{(i)}.\tag{44}$$

The effective covariance is

$$\mathbf{R}_{\text{eff}}^{(i)} = s_R \mathbf{R}_0^{(i)} + \mathbf{J}_p^{(i)} \mathbf{P}_{\text{pos}} \mathbf{J}_p^{(i)\top} + \epsilon_R \mathbf{I}, \quad (45)$$

where $\mathbf{J}_p^{(i)} = \partial[u, v, \rho] / \partial[x, y, z]$ is computed by numerical difference. The time-since-last-valid position uncertainty is

$$\sigma_j = \kappa \left(|v_j| \Delta t + \frac{1}{2} |a_j| \Delta t^2 \right), \quad \mathbf{P}_{\text{pos}} = \text{diag}(\sigma_x^2, \sigma_y^2, \sigma_z^2). \quad (46)$$

The gating statistic is

$$d_i^2 = \boldsymbol{\nu}_k^{(i)\top} \left(\mathbf{R}_{\text{eff}}^{(i)} \right)^{-1} \boldsymbol{\nu}_k^{(i)}. \quad (47)$$

Two thresholds are used:

$$\gamma_{\text{soft}} = \chi_3^2(0.99), \quad \gamma_{\text{hard}} = \chi_3^2(0.999). \quad (48)$$

The rule is

$$\begin{cases} d_i^2 > \gamma_{\text{hard}} : & \text{reject camera block,} \\ \gamma_{\text{soft}} < d_i^2 \leq \gamma_{\text{hard}} : & \text{accept with inflated covariance,} \\ d_i^2 \leq \gamma_{\text{soft}} : & \text{accept normally.} \end{cases} \quad (49)$$

If a camera block is accepted with inflated covariance, both its geometric and tilt covariances are inflated. Thus, roll/pitch observations follow the same camera-level reliability decision.

V. EXPERIMENTS

A. YOLO-OBB Training Results

The generated dataset uses DOTA-style four-point OBB labels. The UAV samples are generated by the weak-prior pipeline. Additional categories and background samples are used to improve robustness in real scenes.

The detector is trained with an input resolution of 640×640 . The training curves in Fig. 6 show stable convergence. The validation result reaches $\text{mAP}@0.5 = 0.692$, and the UAV class reaches $\text{AP}_{50} = 0.973$. This indicates that the weak-prior labels are sufficiently consistent for learning stable UAV OBB direction and scale.

B. Simulation Setup

The MATLAB simulation evaluates whether tilt observations improve short-horizon prediction. The trajectory generator produces a nonlinear three-dimensional motion. Each camera outputs

$$\mathbf{z}_k^{(c)} = \left[u_k^{(c)} \quad v_k^{(c)} \quad \rho_k^{(c)} \quad \eta_{\text{roll},k}^{(c)} \quad \eta_{\text{pitch},k}^{(c)} \right]^\top. \quad (50)$$

Algorithm 2 Tilt-constrained asynchronous multi-camera fusion

Require: Previous estimate, covariance, incoming camera observations

Ensure: Updated state and short-horizon prediction

- 1: Assign observations to Cam1, Cam2, and Cam3 slots.
 - 2: Propagate the augmented state by Δt .
 - 3: **for** each camera slot i **do**
 - 4: **if** camera block is missing **then**
 - 5: Mark camera i unavailable.
 - 6: **else**
 - 7: Predict $[u, v, \rho, \eta_{\text{roll}}, \eta_{\text{pitch}}]$.
 - 8: Compute the Mahalanobis statistic for $[u, v, \rho]$.
 - 9: **if** $d_i^2 > \gamma_{\text{hard}}$ **then**
 - 10: Reject this camera block.
 - 11: **else if** $d_i^2 > \gamma_{\text{soft}}$ **then**
 - 12: Accept with inflated covariance.
 - 13: **else**
 - 14: Accept normally.
 - 15: **end if**
 - 16: **end if**
 - 17: **end for**
 - 18: **if** at least one camera block is accepted **then**
 - 19: Perform the UKF measurement update.
 - 20: **end if**
 - 21: Propagate the updated state to the prediction horizon.
-

Dropouts and false detections are generated by independent camera-level Markov chains. For each camera, $T_i = 1$ means that the true target is detected, and $F_i = 1$ means that a false detection is present. The three-camera detection state is

$$\mathbf{s}_k = \left[T_{1,k} \quad F_{1,k} \quad T_{2,k} \quad F_{2,k} \quad T_{3,k} \quad F_{3,k} \right]^T. \quad (51)$$

The steady-state true detection probability is 0.98, the mean target-loss duration is 30 frames, the steady-state false-detection probability is 0.02, and the mean false-detection duration is 30 frames.

Two settings are compared:

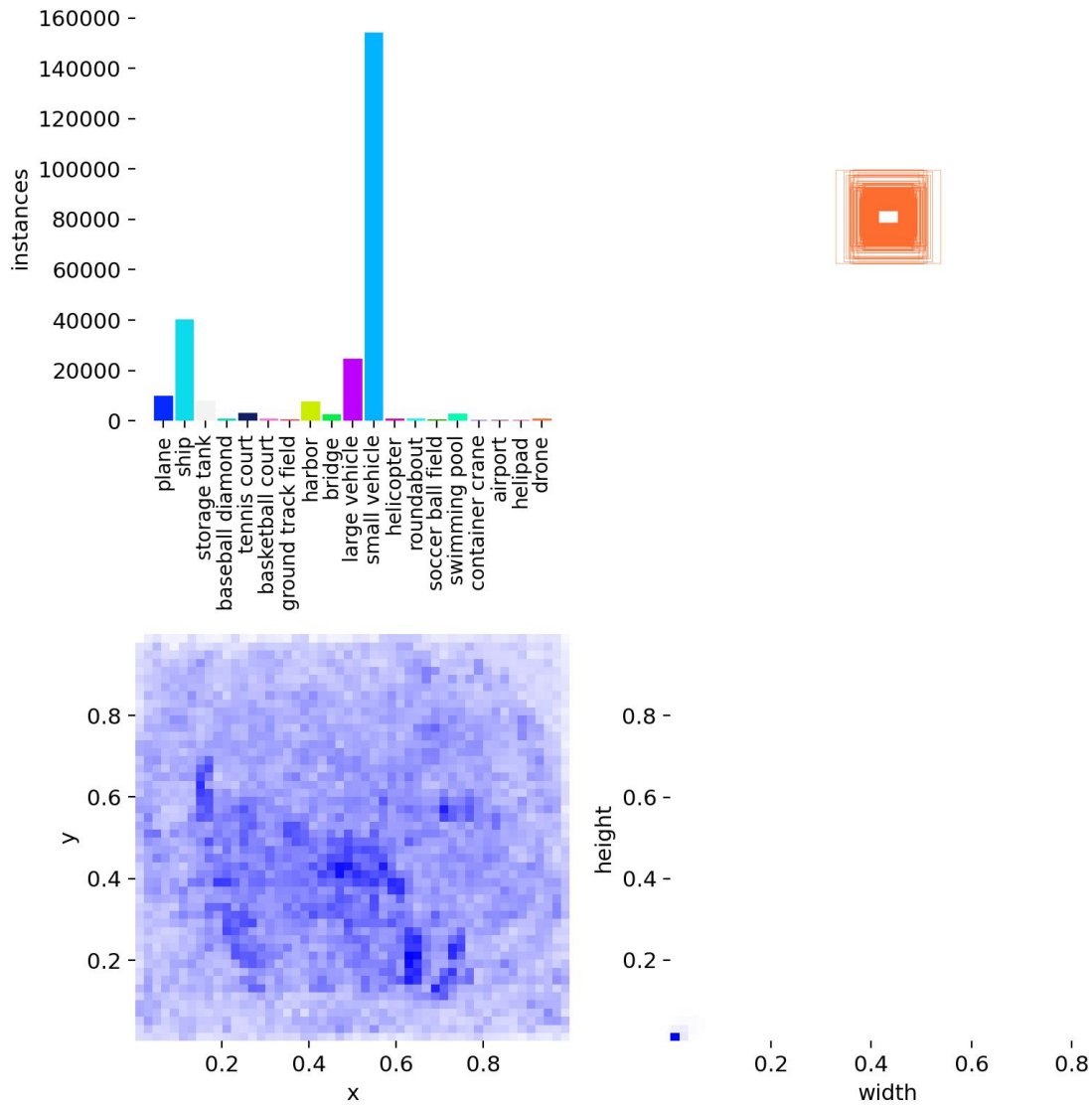


Fig. 4. Class distribution and OBB label statistics of the generated dataset.

- **Baseline:** image position and range are used; roll/pitch observations are disabled.
- **Roll/Pitch:** image position, range, and image-domain roll/pitch are used.

The prediction horizon is $\tau = 0.5$ s. The prediction error is

$$e(t_k) = \|\mathbf{p}_{\text{pred}}(t_k) - \mathbf{p}_{\text{true}}(t_k + \tau)\|_2. \quad (52)$$

C. Simulation Results

Table I summarizes the prediction errors. Adding image-domain roll/pitch observations decreases the cumulative error from 6611.580 m · s to 2594.837 m · s. The RMSE decreases from 1.991 m to 0.821 m,



Fig. 5. Qualitative examples of OBB labels and YOLO-OBB predictions.

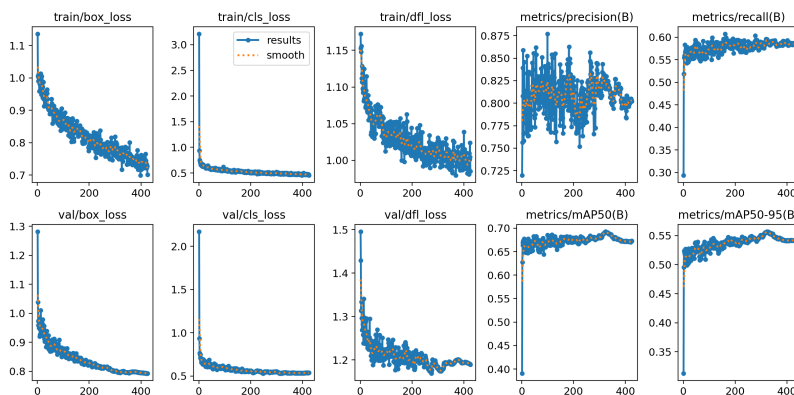


Fig. 6. YOLO-OBB training curves.

and the maximum error decreases from 6.556 m to 3.553 m.

TABLE I
PREDICTION ERROR REDUCTION FROM IMAGE-DOMAIN ROLL/PITCH OBSERVATIONS IN SIMULATION.

Metric	Baseline	Roll/Pitch	Reduction
Cumulative error E_{cum} (m-s)	6611.580	2594.837	60.75%
Mean error \bar{e} (m)	1.838	0.721	60.75%
RMSE (m)	1.991	0.821	58.73%
Maximum error e_{max} (m)	6.556	3.553	45.81%

The simulation verifies the expected mechanism. Image-domain roll/pitch directly constrains the acceleration-related part of the state, reducing prediction lag during maneuvering.

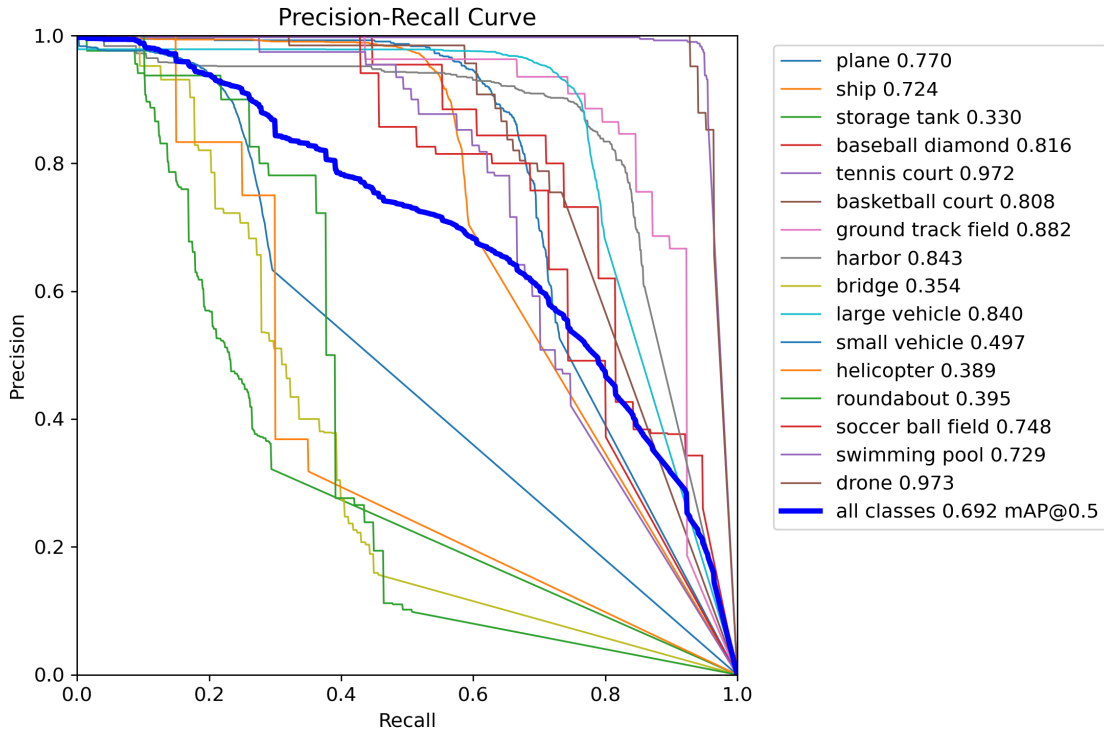


Fig. 7. Validation precision–recall curves and per-class AP₅₀.

D. Real Distributed Multi-Camera Experiment

The real experiment uses one mobile gimbal camera mounted on a quadruped robot and two fixed ground cameras. The mobile camera provides a reconfigurable viewpoint, while the fixed cameras provide stable redundant observations. Each incoming observation is assigned to a fixed camera slot and fused asynchronously.

The real experiment does not use independent high-precision 3D ground truth. Therefore, a self-consistency metric is used. At time t , the state estimated at $t - \tau$ is predicted to t , and the predicted observation is compared with the current observation:

$$e(t) = \sqrt{\frac{1}{|\Omega(t)|} \sum_{j \in \Omega(t)} r_j^2(t)}, \quad (53)$$

where

$$r_j(t) = \begin{cases} \text{wrap}(\hat{z}_j(t|t-\tau) - z_j(t)), & z_j \text{ is an angle,} \\ \hat{z}_j(t|t-\tau) - z_j(t), & z_j \text{ is non-angular.} \end{cases} \quad (54)$$

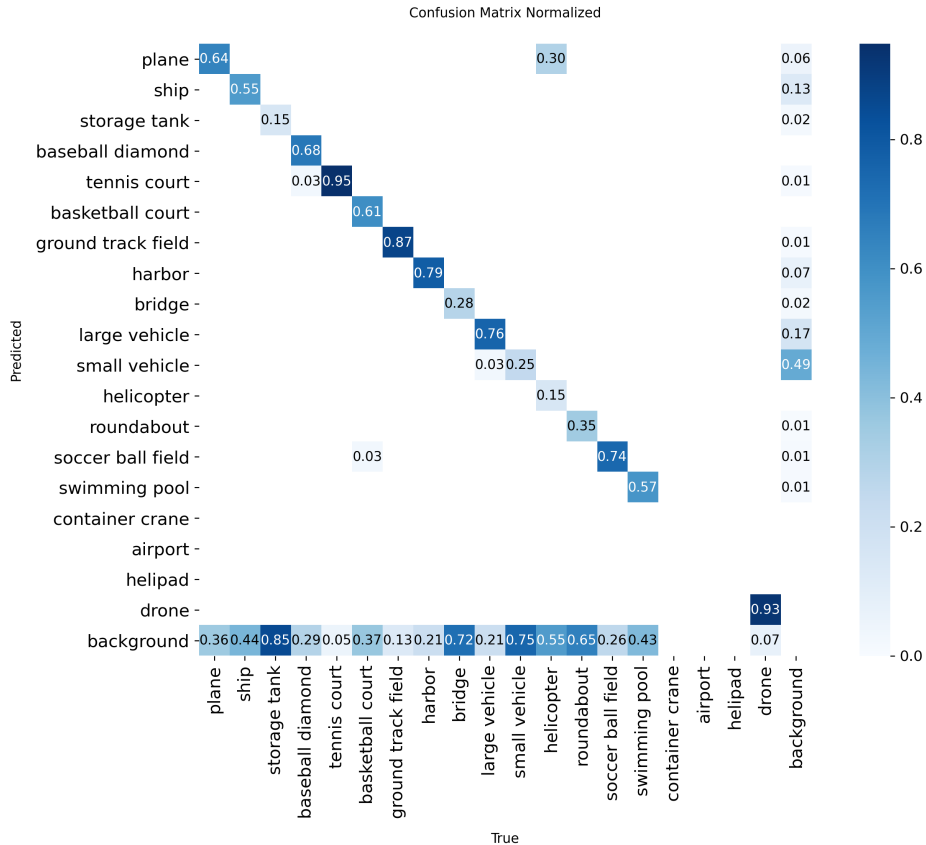


Fig. 8. Normalized confusion matrix on the validation set.

The cumulative self-consistency error is

$$E = \int e(t) dt. \quad (55)$$

Table II shows the result. Enabling roll/pitch observations reduces the cumulative self-consistency error from 203.4518 to 166.6241, corresponding to an 18.10% reduction. The improvement is smaller than in simulation because the real system contains detector jitter, residual extrinsic error, timing mismatch, and camera-dependent observation quality. Nevertheless, the result shows that image-domain tilt remains useful under practical asynchronous multi-camera conditions.

E. Robustness Analysis

The main practical error sources are false detections, dropouts, aggressive maneuvers, and camera-pose inconsistency. False detections are handled by the hard Mahalanobis gate. Moderate residuals after dropouts are handled by covariance widening. Aggressive maneuvers are handled by the tilt-to-acceleration pseudo-observation. Camera-pose inconsistency is handled by the augmented camera attitude states.

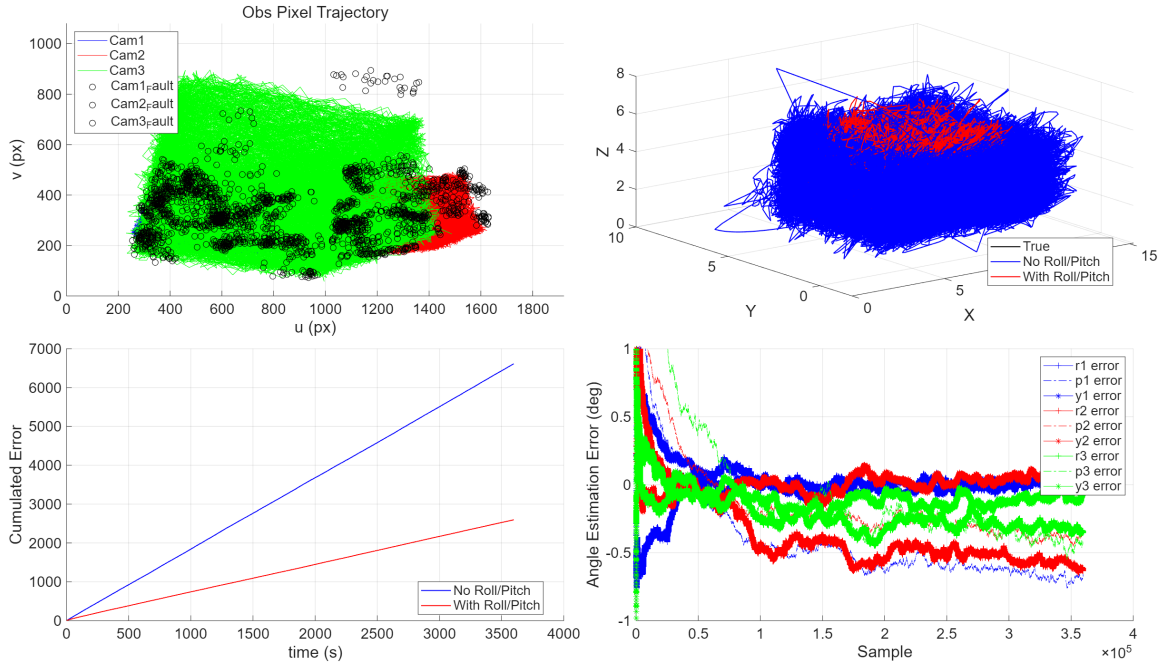


Fig. 9. Overall results of the three-camera asynchronous simulation. Top-left: observed pixel trajectories with false detections. Top-right: 3D trajectory comparison. Bottom-left: cumulative prediction error. Bottom-right: camera Euler-angle estimation error.

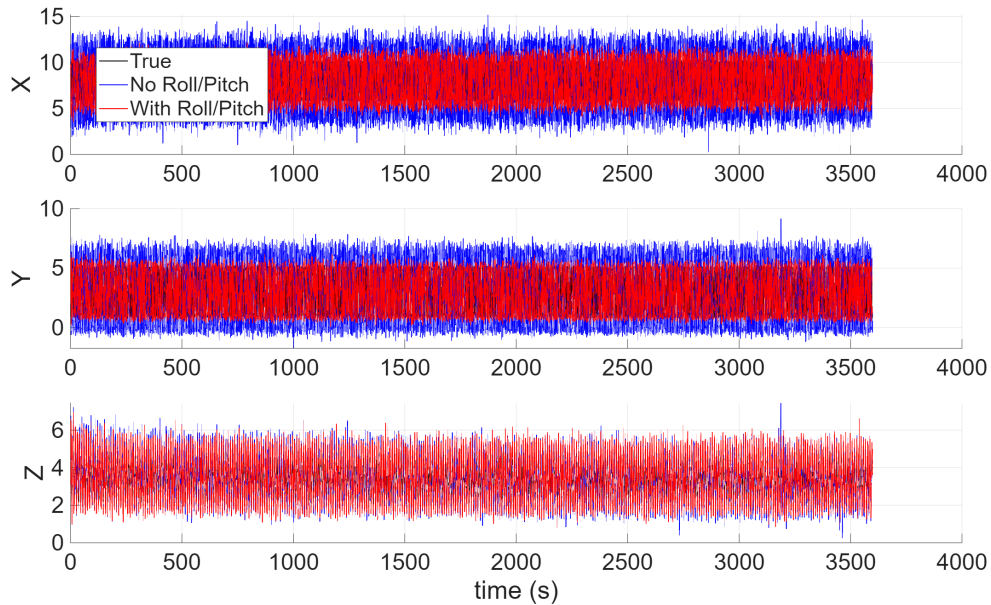


Fig. 10. Time series comparison of 3D position. Black: true trajectory. Blue: baseline without roll/pitch. Red: filter with roll/pitch observations.

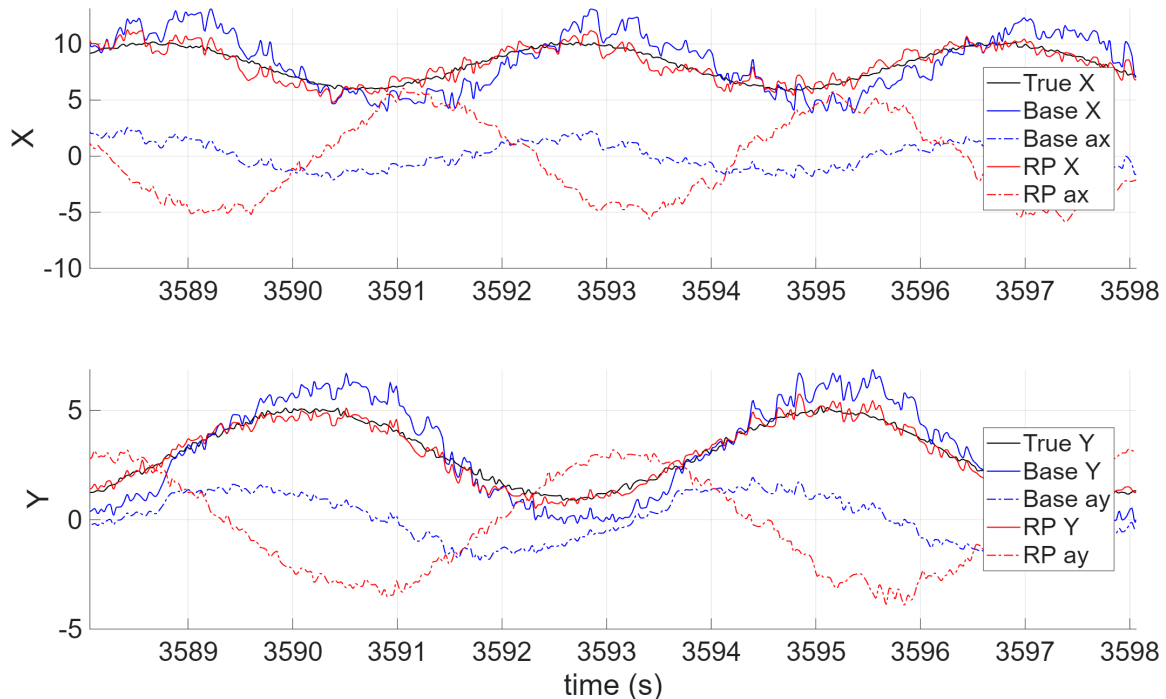


Fig. 11. Position–acceleration comparison in the last 10 s simulation window.

TABLE II

REAL DISTRIBUTED EXPERIMENT: CUMULATIVE SELF-CONSISTENCY PREDICTION ERROR.

Method	Cumulative error E	Relative reduction
Baseline without Roll/Pitch	203.4518	–
Roll/Pitch enabled	166.6241	18.10%

The zoomed maneuver segment illustrates the role of image-domain tilt. Without tilt cues, acceleration is mainly inferred from position and range updates, so it tends to lag. With roll/pitch cues, the filter receives an additional maneuver-related constraint and produces a more responsive acceleration estimate.

VI. CODE AVAILABILITY

The Python implementation of the weak-prior auto-labeling pipeline and YOLO-OBB training workflow is publicly available at

<https://github.com/ShineMinxing/PythonYOLO>

The repository contains motion point extraction, target trajectory tracing, weak observed-angle and YOLO-OBB dataset generation, and YOLO-OBB training scripts.

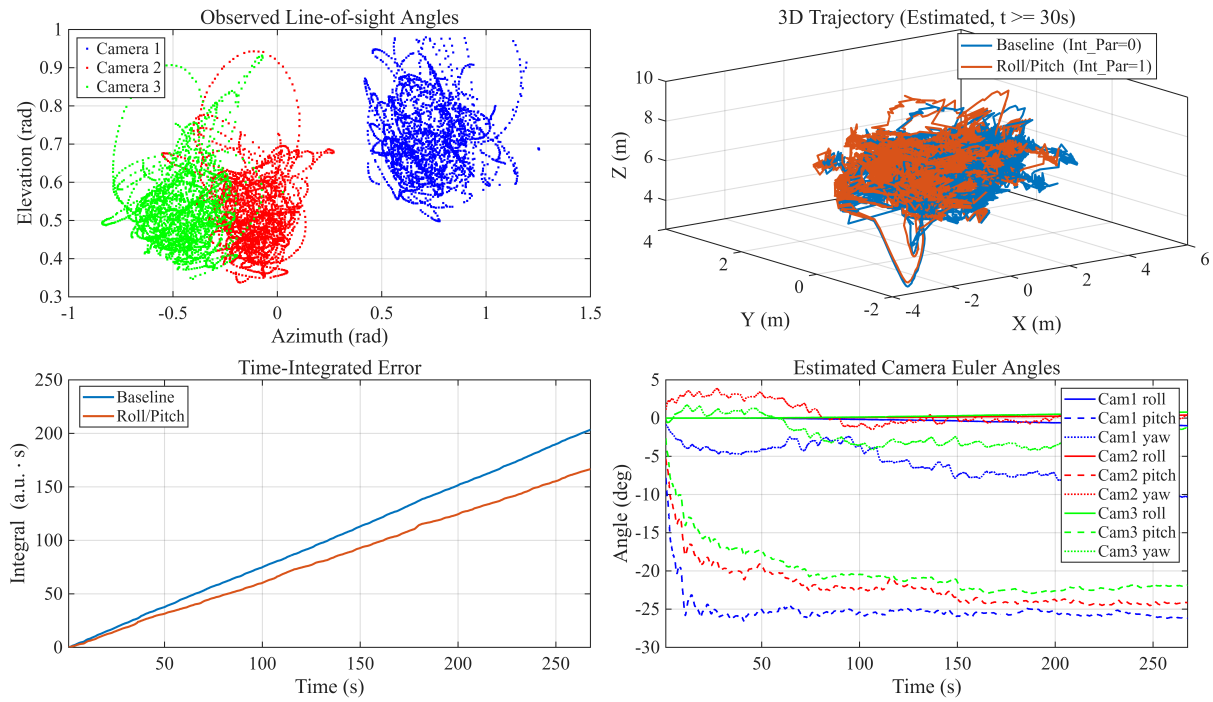


Fig. 12. Overview of distributed fusion with a mobile gimbal camera and two fixed ground cameras. The figure includes line-of-sight observation distribution, 3D trajectory, cumulative error comparison, and estimated camera Euler-angle error states.

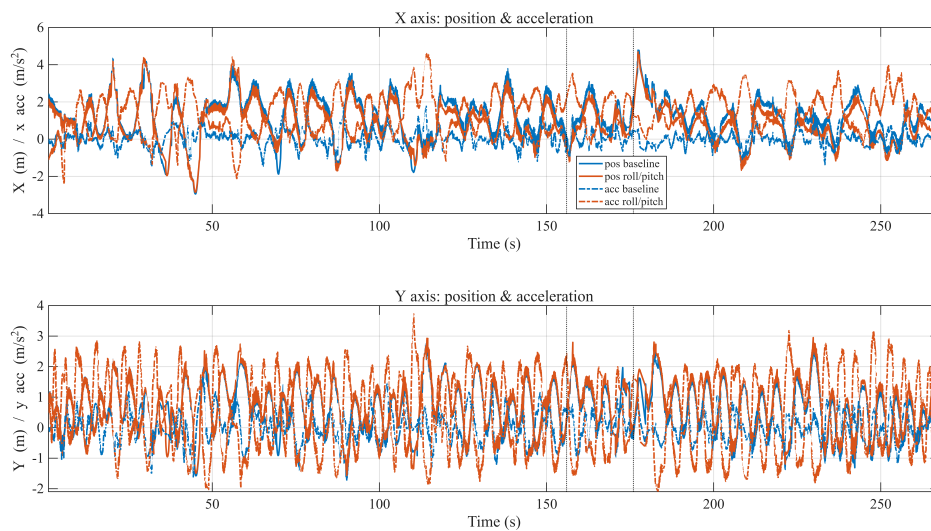


Fig. 13. Distributed fusion position and acceleration comparison on X/Y axes over the full sequence. Solid lines denote position and dash-dot lines denote acceleration. Blue denotes the baseline and red denotes the roll/pitch-enhanced filter.

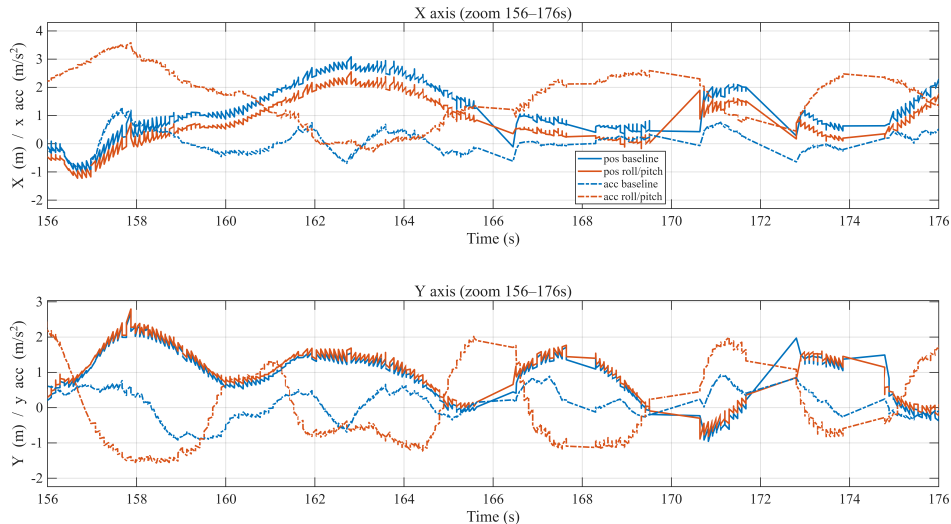


Fig. 14. Zoomed aggressive maneuver segment from 156 to 176 s. With roll/pitch observations, acceleration responds faster and oscillates less, improving short-horizon prediction consistency.

VII. CONCLUSION

This paper presented an image-domain tilt constrained distributed fusion framework for maneuvering UAV tracking. The method uses synchronized video, gimbal IMU, and UAV IMU data to generate weak OBB and image-domain roll/pitch labels, trains a YOLO-OBB detector for online tilt extraction, and introduces the extracted tilt as an acceleration-related pseudo-observation in a nonlinear recursive estimator. For distributed tracking, asynchronous observations from one mobile gimbal camera and two fixed ground cameras are fused with augmented camera attitude states.

The results show that image-domain tilt is a useful low-level maneuver cue. In simulation, it reduces prediction RMSE by 58.73% and cumulative prediction error by 60.75%. In the real multi-camera experiment, it reduces the self-consistency cumulative error by 18.10%. The smaller real-world gain is expected because the real system contains detector jitter, residual extrinsic errors, timing mismatch, and camera-dependent observation quality. Future work will focus on improving tilt recognition stability, estimating time offsets explicitly, and jointly adapting detector confidence, tilt uncertainty, and distributed fusion consistency.

REFERENCES

- [1] S. O. de Macedo, M. Caetano, and R. M. da Costa, “Drone detection in airport environments: A literature review,” *Array*, vol. 28, p. 100511, Dec. 2025.

- [2] S. G. Bahncmiri, M. Ponomarenko, and K. Egiazarian, "Deep Convolutional Autoencoder for Estimation of Nonstationary Noise in Images," in *2019 8th European Workshop on Visual Information Processing (EUVIP)*, Oct. 2019, pp. 238–243.
- [3] B. Qi, S. Zhang, W. Chen, Y. Fu, and B. Ren, "Adaptive Kalman Filters Based on Elliptically Contoured Distributions for Heavy-Tailed and Nonstationary Measurement Noises," *IEEE Transactions on Instrumentation and Measurement*, vol. 74, pp. 1–15, 2025.
- [4] Y. Chen, Y. Cai, Y. Deng, and J. Liu, "Stochastic Event-Triggered Robust Tracking Algorithm Under Nonstationary Heavy-Tailed Noise and Packet Dropouts," *IEEE Transactions on Automation Science and Engineering*, vol. 23, pp. 4428–4441, 2026.
- [5] L. F. R. Moreira, R. Moreira, B. A. N. Travencolo, and A. R. Backes, "Deep learning based image classification for embedded devices: A systematic review," *Neurocomputing*, vol. 623, p. 129402, Mar. 2025.
- [6] J. Qiu, Y. Zhang, Y. Fang, P. Li, and K. Zheng, "Review of Event Camera-Based Target Detection and Tracking Algorithms," *Laser & Optoelectronics Progress*, vol. 62, no. 4, p. 0400004, Feb. 2025.
- [7] Gokila Deepa G, Gomathi S, Aadhitya S, Sujitha R, Sundarrajan M, and M. D. Choudhry, "Optimizing Real-Time Image Processing in Augmented Reality with Low-Latency Edge AI," in *2024 2nd International Conference on Signal Processing, Communication, Power and Embedded System (SCOPEs)*, Dec. 2024, pp. 1–6.
- [8] S. Ren, K. He, R. Girshick, and J. Sun, "Faster R-CNN: Towards Real-Time Object Detection with Region Proposal Networks," *IEEE Transactions on Pattern Analysis and Machine Intelligence*, vol. 39, no. 6, pp. 1137–1149, Jun. 2017.
- [9] V. S. Karthikeya Nalam, V. S. Amar Koushik Tanniru, A. Posani, and M. Suneetha, "Detection and Recognition of Drones using Deep Convolution Neural Networks," in *2022 IEEE 6th Conference on Information and Communication Technology (CICT)*, Nov. 2022, pp. 1–5.
- [10] R. Jain, S. Shrivastav, S. Kakde, and R. Raut, "Performance Comparison of YOLO Algorithms in Drone Detection," in *2024 IEEE International Conference on Smart Power Control and Renewable Energy (ICSPCRE)*, Jul. 2024, pp. 1–6.
- [11] H. J. Al dawasari, M. Bilal, M. Moinuddin, K. Arshad, and K. Assaleh, "Pre-trained Deep Learning Networks for Advanced Visible Imagery Drone Detection and Recognition," in *2023 IEEE 15th International Conference on Computational Intelligence and Communication Networks (CICN)*, Dec. 2023, pp. 316–320.
- [12] V. Taware, M. Bhandare, S. Bhirud, S. Sawant, and A. Joshi, "Small Object Detection and Classification Using YOLO on Multi-Dataset Drone Imagery," in *2025 IEEE Pune Section International Conference (PuneCon)*, Dec. 2025, pp. 1–6.
- [13] J. Han, R. Cao, A. Brighente, and M. Conti, "Light-YOLOv5: A Lightweight Drone Detector for Resource-Constrained Cameras," *IEEE Internet of Things Journal*, vol. 11, no. 6, pp. 11 046–11 057, Mar. 2024.
- [14] S. A. Dogan, J. Walatkiewicz, S. Tout, O. Darwish, and O. Spantidi, "Experimental Analysis of Fine-Tuned Drone Detection YOLO Models," in *2025 1st International Conference on Secure IoT, Assured and Trusted Computing (SATC)*, Feb. 2025, pp. 1–5.
- [15] J. Singh, K. Sharma, M. Wazid, A. K. Das, and A. V. Vasilakos, "An Ensemble-Based IoT-Enabled Drones Detection Scheme for a Safe Community," *IEEE Open Journal of the Communications Society*, vol. 4, pp. 1946–1956, 2023.
- [16] A. F. Serageldin, H. A. Elsayed, and L. Abdel-Hamid, "Real-Time UAV Detection Using an Enhanced YOLO v8 Model," in *2025 42nd National Radio Science Conference (NRSC)*, vol. 1, May 2025, pp. 193–201.
- [17] D. Teets and K. Whitehead, "The Discovery of Ceres: How Gauss Became Famous," *Mathematics Magazine*, vol. 72, no. 2, pp. 83–93, Apr. 1999.
- [18] N. Wiener, "The Linear Predictor for a Single Time Series," in *Extrapolation, Interpolation, and Smoothing of Stationary Time Series: With Engineering Applications*. MIT Press, 1964, pp. 56–80.

- [19] R. E. Kalman, "A new approach to linear filtering and prediction problems," *Journal of Basic Engineering*, vol. 82, no. 1, pp. 35–45, Mar. 1960.
- [20] Y. Bar-Shalom, X. R. Li, and T. Kirubarajan, *Estimation with Applications to Tracking and Navigation: Theory Algorithms and Software*. John Wiley & Sons, 2001.
- [21] S. J. Julier and J. K. Uhlmann, "A new extension of the kalman filter to nonlinear systems," in *Signal Processing, Sensor Fusion, and Target Recognition VI*, vol. 3068. Bellingham: Spie - Int Soc Optical Engineering, 1997, pp. 182–193.
- [22] E. Wan and R. Van Der Merwe, "The unscented kalman filter for nonlinear estimation," in *Proceedings of the IEEE 2000 Adaptive Systems for Signal Processing, Communications, and Control Symposium (Cat. No.00EX373)*, Oct. 2000, pp. 153–158.
- [23] R. van der Merwe, A. Doucet, N. de Freitas, and E. Wan, "The Unscented Particle Filter," in *Advances in Neural Information Processing Systems*, vol. 13. MIT Press, 2000.
- [24] S. Julier and J. Uhlmann, "Unscented filtering and nonlinear estimation," *Proceedings of the IEEE*, vol. 92, no. 3, pp. 401–422, Mar. 2004.
- [25] I. Arasaratnam and S. Haykin, "Cubature kalman filters," *IEEE Transactions on Automatic Control*, vol. 54, no. 6, pp. 1254–1269, Jun. 2009.
- [26] N. Gordon, D. Salmond, and A. Smith, "Novel-Approach to Nonlinear Non-Gaussian Bayesian State Estimation," *IEE PROCEEDINGS-F RADAR AND SIGNAL PROCESSING*, vol. 140, no. 2, pp. 107–113, Apr. 1993.
- [27] D. Fox, S. Thrun, W. Burgard, and F. Dellaert, "Particle Filters for Mobile Robot Localization," in *Sequential Monte Carlo Methods in Practice*, ser. Statistics for Engineering and Information Science, A. Doucet, N. de Freitas, and N. Gordon, Eds. New York, NY: Springer, 2001, pp. 401–428.
- [28] H. Blom and Y. Barshalom, "The Interacting Multiple Model Algorithm for Systems with Markovian Switching Coefficients," *IEEE TRANSACTIONS ON AUTOMATIC CONTROL*, vol. 33, no. 8, pp. 780–783, Aug. 1988.
- [29] X. Fu, Y. Jia, J. Du, and F. Yu, "New interacting multiple model algorithms for the tracking of the manoeuvring target," *IET CONTROL THEORY AND APPLICATIONS*, vol. 4, no. 10, pp. 2184–2194, Oct. 2010.
- [30] T. Q. Truong, "Exploration of adaptive filters for target tracking in the presence of model uncertainty," in *2010 Sixth International Conference on Intelligent Sensors, Sensor Networks and Information Processing*. IEEE, Dec. 2010, pp. 1–6.
- [31] P. J. Huber, "Robust Estimation of a Location Parameter," in *Breakthroughs in Statistics*, S. Kotz and N. L. Johnson, Eds. New York, NY: Springer New York, 1992, pp. 492–518.
- [32] G. Zames, "Feedback and optimal sensitivity: Model reference transformations, multiplicative seminorms, and approximate inverses," *IEEE Transactions on Automatic Control*, vol. 26, no. 2, pp. 301–320, Apr. 1981.
- [33] A. H. Sayed, "A framework for state-space estimation with uncertain models," *IEEE TRANSACTIONS ON AUTOMATIC CONTROL*, vol. 46, no. 7, pp. 998–1013, Jul. 2001.
- [34] S. S. Ge and J. Wang, "Robust adaptive tracking for time-varying uncertain nonlinear systems with unknown control coefficients," *IEEE TRANSACTIONS ON AUTOMATIC CONTROL*, vol. 48, no. 8, pp. 1463–1469, Aug. 2003.
- [35] H.-n. Jiang and Y.-l. Cai, "Robust Gaussian-sum ensemble Kalman filter and its application in bearings-only tracking," *Kongzhi Lilun yu Yingyong = Control Theory & Applications*, vol. 35, no. 2, Feb. 2018.
- [36] H. Wu, S.-X. Chen, B.-F. Yang, and K. Chen, "Robust cubature Kalman filter target tracking algorithm based on generalized M-estiamtion," *ACTA PHYSICA SINICA*, vol. 64, no. 21, p. 218401, Nov. 2015.
- [37] J. Ma and X. Guo, "Combination of IMM Algorithm and ASTRWCKF for Maneuvering Target Tracking," *IEEE Access*, vol. 8, pp. 143 095–143 103, 2020.

- [38] Z. Tang, Y. Liu, T. Liu, X. Xu, and J. Liu, "Adaptive Weighted Ridge Regression Estimator for Time-Varying Sensitivity Identification," *IEEE Transactions on Power Systems*, vol. 39, no. 1, pp. 2377–2380, Jan. 2024.
- [39] R. Liu, Y. Xiao, Z. Li, and H. Cao, "Research on the anti-UAV distributed system for airports : YOLOv5-based auto-targeting device," in *2022 3rd International Conference on Computer Vision, Image and Deep Learning & International Conference on Computer Engineering and Applications (CVIDL & ICCEA)*, May 2022, pp. 864–867.
- [40] G. Bledt, M. J. Powell, B. Katz, J. Di Carlo, P. M. Wensing, and S. Kim, "MIT Cheetah 3: Design and Control of a Robust, Dynamic Quadruped Robot," in *2018 IEEE/RSJ International Conference on Intelligent Robots and Systems (IROS)*, Oct. 2018, pp. 2245–2252.
- [41] O. Villarreal, V. Barasuol, P. M. Wensing, D. G. Caldwell, and C. Semini, "MPC-based Controller with Terrain Insight for Dynamic Legged Locomotion," in *2020 IEEE International Conference on Robotics and Automation (ICRA)*, May 2020, pp. 2436–2442.
- [42] R. Grandia, F. Jenelten, S. Yang, F. Farshidian, and M. Hutter, "Perceptive Locomotion through Nonlinear Model Predictive Control," Aug. 2022.